Journal of Applied Geophysics 246 (2026) 106077

Contents lists available at ScienceDirect

Journal of Applied Geophysics

journal homepage: www.elsevier.com/locate/jappgeo

Three-dimensional anisotropic modelling of magnetotelluric data to determine the boundary between cap rock and reservoir formation: A case study of the Sarab field, Iran

Mohammad Filbandi Kashkouli [a,*], Matthew J. Comeau [b,*], Milad Farshad [c], Abolghasem Kamkar-Rouhani [a]

[a] Department of Mining, Petroleum and Geophysics, Shahrood University of Technology, Shahrood, Iran
[b] Department of Geoscience and Engineering, Delft University of Technology, Delft, the Netherlands
[c] Previously MINES Paris PSL, Paris, France

ARTICLE INFO

Keywords:
Electrical Resistivity
Magnetotellurics
Anisotropy
Reservoir
Cap Rock
Evaporite

ABSTRACT

Reservoirs of interest for resource exploration, including geothermal and hydrocarbon reservoirs, commonly have an impermeable cap, which traps fluids below. Identifying this boundary is important for resource development. The cap rock for hydrocarbon reservoirs in southwest Iran contains evaporites and thus some geophysical exploration methods, specifically seismic reflection, have faced problems recovering subsurface information in this environment. As an alternative, we generate an electrical resistivity model from magnetotelluric (MT) data. Furthermore, we consider three-dimensional triaxial electrical anisotropy, which is rarely done. The study objectives are to a) define and map the boundary between the cap rock and the principal reservoir, b) characterize geological and tectonic formations in the area, and c) analyze the tectonic factors influencing the evolution of the region. A total of 359 MT measurements were acquired across the Sarab field in an array consisting of five profiles separated by >2000 m with a measurement spacing of >200 m. Transient electromagnetic (TEM) measurements were co-located with the MT measurements at 181 locations and used to correct for static shifts. Isotropic and anisotropic inversions of the MT data were performed, using all impedance tensor elements. The anisotropic electrical resistivity model exhibits both a significantly better alignment with the depths of geological formations known from drilling data and a better fit to the data. Therefore, the boundary between the primary cap rock and principal reservoir, the Gachsaran and Asmari formations, is defined and mapped across the survey area. In addition, major tectonic and fault-related features in the region are identified.

1. Introduction

The use of geophysical methods is an essential requirement for a better understanding of subsurface structures, and this is also true for characterizing regions for resource exploration, including geothermal and hydrocarbon reservoirs (Johansen et al., 2005; Constable and Weiss, 2006; Liang et al., 2012; Sun et al., 2015; Rajab and Tarazi, 2017; Al-Farhan et al., 2019). The seismic reflection method is a standard exploration tool; however, despite its successes, there are situations where the seismic reflection method cannot provide reliable information about subsurface structures (e.g., Oz Yilmaz, 2001). These situations can occur, for example, when a high velocity layer or a plastic layer causes signal attenuation and/or de-focusing of the seismic waves (e.g., Zhdanov et al., 2011). In these situations, a successful exploration program should take alternative and/or complementary approaches (Strack et al., 1991; Martini et al., 2005; Jones and Davison, 2014).

In recent decades, among various geophysical methods, electromagnetic (EM) methods have received particular attention to complement seismic data suffering from the shortcomings listed above (e.g., Zhdanov et al., 2011). Various EM methods have been used in the exploration for resources, and, in particular, the magnetotelluric (MT) method — which allows deep soundings — is efficient and inexpensive in comparison to seismic methods (Watts and Pince, 1998; Matsuo and Negi, 1999; Travassos and Menezes, 1999; Hoversten et al., 2000; Hoversten et al., 1996; Martini et al., 2005; Xiao and Unsworth, 2006; Zhang et al., 2014; Strack, 2014; Mansoori et al., 2015, 2016;

* Corresponding authors.
E-mail addresses: kashkoulimohammad@gmail.com (M. Filbandi Kashkouli), M.J.Comeau@tudelft.nl (M.J. Comeau).

https://doi.org/10.1016/j.jappgeo.2025.106077
Received 17 September 2025; Received in revised form 21 December 2025; Accepted 23 December 2025
Available online 23 December 2025

Sarvandani et al., 2017).

The Sarab field is located in the Gachsaran region, southwest Iran, and is the second largest hydrocarbon-producing region in Iran (e.g., Murris, 1980; Edgell, 1996). The Gachsaran Formation is characterized by significant lithological diversity — predominantly composed of cyclic deposits of marine carbonates, nodular gypsum-anhydrite, and red or variegated marls — and thickness variations, due to tectonic processes such as faulting and thrusting (Gill and Ala, 1972; Mahmoodabadi, 2020). While the formation's original sedimentary thickness is uncertain, estimates suggest it can reach up to 3500 m in certain areas (e.g., James and Wynd, 1965). Towards the basin margins, clastic facies dominate with thicker limestone and marl intervals, whereas the basin centre features more expansive evaporite deposits and thinner clastic layers. These variations reflect the asymmetric basin's depositional environment, with greater subsidence and evaporitic activity centralizing halite and anhydrite deposition (Gill and Ala, 1972; Mahmoodabadi, 2020). A map of the geological formations in the study area is shown in Fig. 1 and an example of a lithostratigraphic column for the Gachsaran formation is shown in Fig. 2.

The existence of evaporites in the formation acts to reduce the quality of seismic data, creating challenges for exploration. In terms of electrical resistivity, there is a large contrast between the cap rock formation (Gachsaran) and the reservoir layer below it (the Asmari formation), and thus electrical methods can provide useful information (e.g., Key et al., 2006; Zhdanov et al., 2011; Moorkamp et al., 2016). In recent years it has become increasingly clear that subsurface electrical anisotropy — that is, a dependence of the electrical resistivity with direction — is not uncommon and is associated with the processes that shape sedimentary basins and tectonic structures (e.g., Lee et al., 2024). Layering, preferential mineral orientation, aligned fractures, and fault-related deformation can all produce electrical anisotropy (whether on a micro or macro scale) and influence MT responses (e.g., Martí, 2014). Ignoring anisotropy may lead to artefacts in isotropic models or to a misplacement of formation boundaries (Bedrosian et al., 2019; Kong et al., 2021; Lee et al., 2024). In regions dominated by evaporites the potential for electrical anisotropy is particularly high because the ductile flow of salt and fault-controlled deformation introduces inherent fabrics and heterogeneity in the subsurface that act to preferentially guide electrical currents (e.g., Melendez Martinez and Schmitt, 2013). Therefore, by explicitly incorporating electrical anisotropy into subsurface models, it is not only possible to improve the fit between modelled and observed data but also to obtain a more geologically realistic model.

The purpose of this study is to generate electrical resistivity models from MT data in order to identify the distribution of different geological formations, especially the Gachsaran cap rock and Asmari reservoir formations, and to characterize the (controlling) tectonic structures in the area of the Sarab field. Therefore, data from the Sarab field is used as a case study to show that addressing electrical anisotropy is not merely a subtle refinement of standard practice, but is an essential step towards reducing uncertainty in subsurface imaging and reservoir exploration.

2. Geological background

The vast majority of hydrocarbon reservoirs in Iran are located in the Zagros region (Motiei, 1995). The region was formed by continuous sedimentation, with only minor interruptions, from the Triassic to the Miocene periods (e.g., Sherkati and Letouzey, 2004). Lack of volcanic and metamorphic phenomena, low scattering of Paleozoic rock outcrops, and a large number of relatively big anticlines along small synclines are other geological features of the Zagros region. The Zagros region is located in the western and southwestern parts of Iran, on the eastern coast of the Persian Gulf. It has a northwest-southeast geological trend and extends for more than 1500 km.

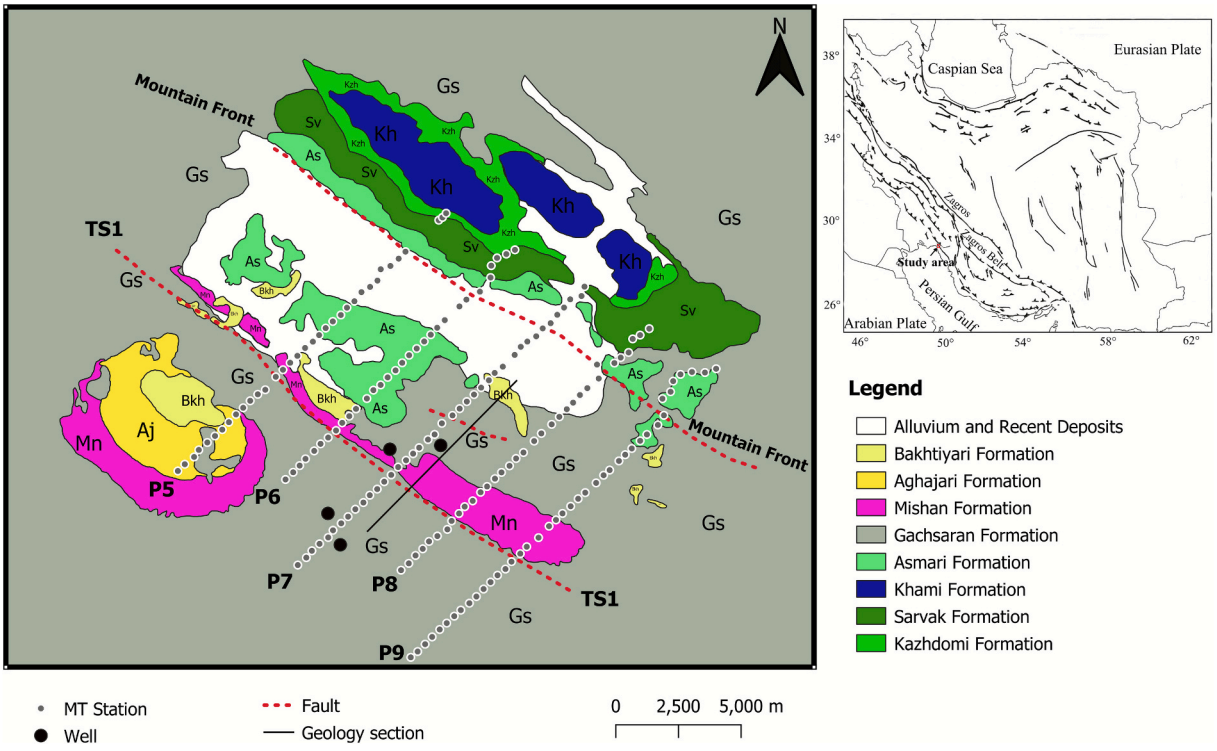

Fig. 1. Map of the study area. Geological formations are coloured. The Mountain Front Fault, the TS1 fault, and the TS2 fault are marked with dashed red lines. A geological section runs along the thin black line. The locations of several drilling wells are marked with black dots. MT + TEM measurement locations are marked with grey circles. Map adapted from O'B Perry and Setudehnia (1966) and Narimani et al. (2012). The inset map shows the tectonic setting (modified from Filbandi Kashkouli et al., 2025) with the red square indicating the study area. (For interpretation of the references to colour in this figure legend, the reader is referred to the web version of this article.)

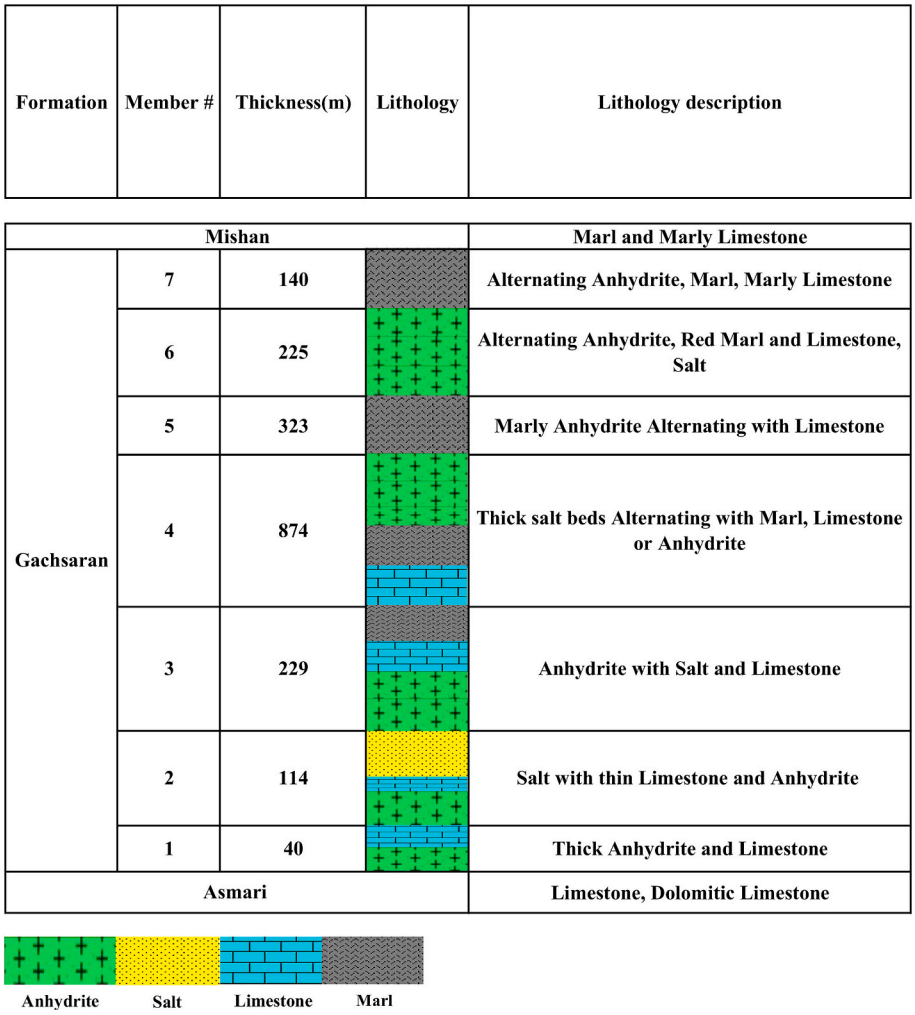

Fig. 2. An example of a lithostratigraphic column for the Gachsaran Formation, prepared in the Rag-e Sefid field (modified from Mahmoodabadi, 2020).

The Zagros region is located on the boundary of the Eurasian and Arabian continental plates and was formed by collision and orogeny during the Cenozoic era (e.g., Takin, 1972; Agard et al., 2005). A large number of parallel folds along the northwest-southeast direction were formed by the collision. They are now seen as anticlines and mountains with high peaks reaching up to 3600 m above sea level. Most of the hydrocarbon reservoirs in the Zagros basin are related to calcareous and carbonate reservoirs (Motiei, 1995). The most important reservoirs are those embedded in the Asmari Formation of Oligocene-Miocene age, followed by the Sarvak Formation (below; part of the wide-spread Bangestan Group) with Cretaceous age (Sherkati and Letouzey, 2004).

In fact, the Asmari Formation contains one of the largest hydrocarbon reservoirs in the world, varying in thickness from a few meters to over 500 m (James and Wynd, 1965; Colman-Sadd, 1978). This formation is mainly composed of dense limestone and dolomite. Above the upper horizon of the Asmari Formation lies the Gachsaran Formation, which contains anhydrite, marl, salt, and a small amount of limestone and shale. It covers more than 90 % of the study area and, according to Motiei (1995), the evaporites in the formation make it an ideal cap rock for preserving the hydrocarbon reservoirs of the Asmari Formation below, due to their very low permeability and porosity.

In this region, the most significant structural feature is the Mountain Front Fault (MFF) (Falcon, 1961; Berberian, 1995), which is located in the northeastern part of the study area (see the map in Fig. 1). The TS1 fault is present in the southwestern part of the study area (Narimani et al., 2012) and a small segment known as the TS2 fault is located in the central part of the study area. The Mountain Front Fault, which is primarily a thrust fault, is one of the key tectonic structures in the Zagros region, marking the boundary between the Zagros Fold-Thrust Belt (to the north; with evidence for thin-skinned and thick-skinned deformation) and the Khuzestan Basin sedimentary plains (to the south) (e.g., Falcon, 1961; Berberian, 1995). Additionally, this fault is considered the main basement fault, characterized by strong topographic variations and structural prominence along its length, serving as the primary focus of major seismic activity (Berberian, 1995; Talebian and Jackson, 2002). The influence of the Mountain Front Fault in the central Zagros (Izeh and Dezful embayment) has been well studied (e.g., Sherkati and Letouzey, 2004; McQuarrie, 2004; Sepehr et al., 2006).

A notable elevation difference is observed across the fault, reaching up to 600 m within a horizontal distance of approximately 500–1500 m. Several studies have attributed this surface elevation difference to basement uplift in the hanging wall (Sherkati and Letouzey, 2004; Sepehr et al., 2006). The topographic and structural front of the fault, with its irregular geometry, reflects embayments and salients along its trace (Sherkati and Letouzey, 2004). The absence of surface thrusting and the limited availability of high-quality seismic data along the fault have complicated its interpretation (Narimani et al., 2012). Berberian (1995) referred to concealed segments of this thrust fault, with lengths ranging between 15 and 115 km, extending over a total length of 1350 km along the Zagros Belt. McQuarrie (2004) attributed the formation of this fault to the accumulation of Hormuz Salt beneath the Zagros hinterland and the Fars Arc, proposing that this thrust fault exhibits a ramp-

flat geometry in the Fars Arc and the Dezful Embayment.

The TS1 fault is located in the footwall of the Mountain Front Fault, with a roughly parallel orientation, trending approximately N127°E. This fault is predominantly covered by alluvial deposits; however, careful field observations can confirm the presence of this thrust fault. The TS1 Fault has, in places, caused the Gachsaran Formation to be thrust over the Mishan Formation (Narimani et al., 2012). The TS2 Fault, trending approximately N125°E, is located in the footwall of the Mountain Front Fault, approximately 4 km away from it. This fault has a limited surface exposure in the study area and is largely covered by alluvial deposits in various sections. A significant portion of the TS2 Fault passes through the Gachsaran Formation (Narimani et al., 2012).

3. Data and method

3.1. Basics of the MT method

The MT method is a passive, frequency-domain electromagnetic method (Tikhonov, 1950; Cagniard, 1953). The natural sources for MT arise from external sources in the form of geomagnetic pulsations (complex interactions between the solar wind and the Earth's magnetosphere and ionosphere) and atmospheric electrical activities (including worldwide lightning discharges, which propagate in the Earth-ionosphere waveguide), providing signals in a broad frequency range (e.g., 10^{-4} to 10^{4} Hz). By utilizing this wide range of frequencies, MT surveys can probe different depths of the Earth's subsurface.

The ratio of the components of the measured horizontal electric and magnetic fields forms a complex impedance tensor **Z**, a transfer function, as follows:

$$\begin{bmatrix} E_x(\omega) \\ E_y(\omega) \end{bmatrix} = \begin{bmatrix} Z_{xx}(\omega) & Z_{xy}(\omega) \\ Z_{yx}(\omega) & Z_{yy}(\omega) \end{bmatrix} \begin{bmatrix} H_x(\omega) \\ H_y(\omega) \end{bmatrix}. \quad (1)$$

Where x and y are perpendicular directions (e.g., northwards and eastwards), E_x and E_y denote the electric field components, H_x and H_y denote the magnetic field components, and ω is the angular frequency ($\omega = 2\pi f$).

The apparent resistivity and impedance phase are effectively obtained through the magnitude and argument of the impedance tensor, respectively. A common representation is as follows, the apparent resistivity (units of Ωm) is determined from:

$$\rho_{a,ij}(\omega) = \frac{1}{\mu_0 \omega} |Z_{ij}(\omega)|^2, \quad (2)$$

and the impedance phase (units of °) is obtained from:

$$\phi_{ij}(\omega) = \tan^{-1} \frac{Im(Z_{ij}(\omega))}{Re(Z_{ij}(\omega))}, \quad (3)$$

where ij denotes the respective elements of the impedance tensor and μ_0 is the magnetic permeability.

3.2. Acquisition and processing of MT data

MT data at 359 stations, in an array of 12 km by 18 km, were collected in 2013. They had an average spacing of approximately 200 m along five profiles, each separated by 2000–3000 m. The profiles had a southwest-northeast orientation (i.e., approximately N45°E) so that they were nearly orthogonal to the principal geological structures, including the trend of the Zagros Fold and Thrust Belt (see Fig. 1). The MT data were measured in two perpendicular directions (North and East). Afterwards, the data were mathematically rotated to a preferred coordinate system. We define the x- and y-directions as along the profiles and across the profiles (with the latter corresponding to approximately along the principal regional geological structures).

MT data were acquired in the range of 0.003–3000 s over a recording time of 12–15 h. Time series processing of the MT data was performed using the SSTM software provided by Phoenix Geophysics Canada based on standard robust processing techniques (e.g., Jones et al., 1989). A remote reference site (located ~100 km from the survey area) was used to eliminate uncorrelated noise and improve data quality (e.g., Jones et al., 1989).

The data were typically of high quality. See Fig. S1 of the Supplementary Material for apparent resistivity and impedance phase curves for all sites. At some sites, noisy long period data was removed. A handful of sites displayed out-of-quadrant phase responses. The causes of out-of-quadrant phase responses can be diverse but are thought to depend on local geological factors; they may arise from complex subsurface structures, such as heterogeneities or strong resistivity contrasts, and, in some cases, electrical anisotropy can also play a role in producing this effect (e.g., Heise et al., 2006; Martí, 2014). In this dataset, the out-of-quadrant phase responses were located within the footwall of the mountain-front fault and were attributed to the associated strong lateral resistivity contrasts.

The range in apparent resistivity recorded at the highest frequency varied from 1 Ωm to 1000 Ωm (see Fig. S1 of the Supplementary Material). This was, in part, attributed to static shift effects. Galvanic distortion effects, that are caused by near-surface resistivity structure at a small spatial length scale, can cause a constant, frequency-independent shift in the local apparent resistivity sounding curve, known as a static shift (e.g., Jones et al., 1989). To correct the static shifts observed in the MT measurements, co-located transient electromagnetic (TEM) soundings at 181 sites with an average spacing of 450–600 m were acquired with instruments from Phoenix Geophysics Canada. These were acquired within a time window of 0.1–10 ms.

An apparent resistivity model was generated from the TEM data with the WinGLink software suite from Geosystem SRL. When the TEM model and the MT apparent resistivity data at the highest frequency (lowest period) did not match, a correction — that is, a constant scaling factor for the apparent resistivity amplitude — was computed for the MT data. For about half of the MT measurements, a match with the TEM model was observed and no correction was required (see Fig. S1b of the Supplementary Material). Fig. 3 shows the (corrected) data for several representative measurement sites as apparent resistivity and impedance phase curves.

Fig. 4 presents the MT data for each measurement location, displayed as pseudo-sections along five profiles with distance on the horizontal axis and period on the vertical axis. The impedance tensor components are presented as apparent resistivity and impedance phase. The Z_{xy} and Z_{yx} components appear to have strong differences; this suggests the presence of complex structures. Pseudosections of the Z_{xx} and Z_{yy} components are provided in Fig. S2 of the Supplementary Material. For periods greater than about 1 s the phase decreases below 45°, indicating an increasing electrical resistivity at depth, which is attributed to the principal reservoir of the Asmari Formation.

3.3. MT data analysis

It is crucial to determine the dimensionality of subsurface structures by analysing the MT data, as this will determine the level of complexity required for the inversion. Dimensionality analysis will determine whether the resistivity of the Earth must be modelled as 1D, 2D, or 3D; that is, in which direction the resistivity changes, only in the vertical direction, vertically and along one horizontal axis (across the geoelectric strike), or vertically and in two horizontal directions. There are various methods for dimensionality and directionality analysis of MT data. We use the distortion-free phase tensor (PT) (Caldwell et al., 2004) and the resistivity phase tensor (RPT) (Hering et al., 2019) in this work.

The phase tensor is characterized by the magnitudes of the maximum phase (ϕ_{max}), minimum phase (ϕ_{min}), and values of α and β, which represent the main direction of the shape axis and the skew angle, respectively. The phase tensor can be graphically represented by ϕ_{max},

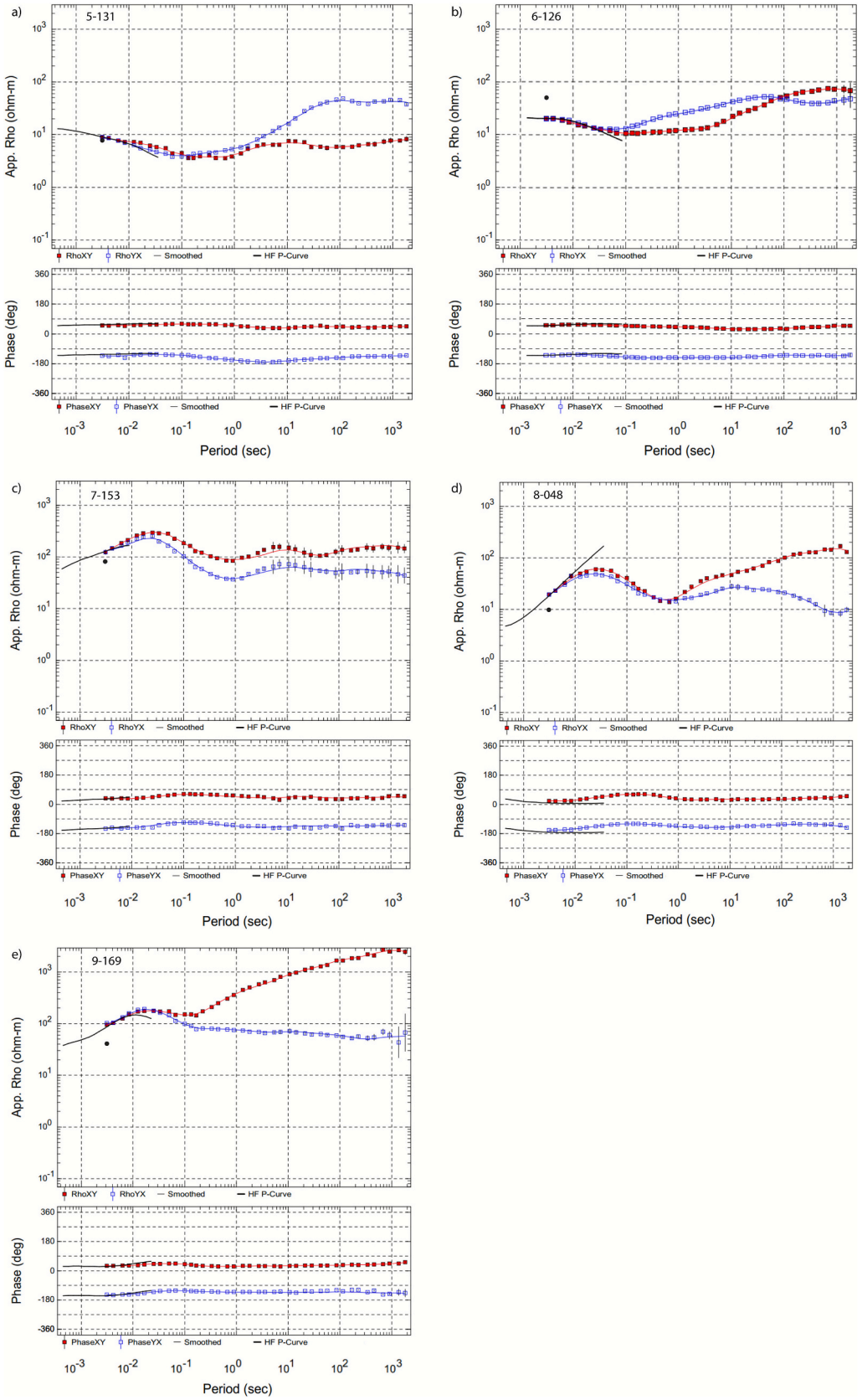

Fig. 3. Apparent resistivity (top) and impedance phase (bottom) curves for a representative site near the centre of each profile (a–e). The MT data is shown as coloured points (red, XY, and blue, YX). The TEM-derived apparent resistivity is indicated with black lines. Co-located TEM measurements were used to correct static shifts in the MT soundings (i.e., to compute a constant scaling factor for the apparent resistivity amplitudes). The black dots mark the apparent resistivity of the uncorrected MT soundings at the lowest period (highest frequency). (For interpretation of the references to colour in this figure legend, the reader is referred to the web version of this article.)

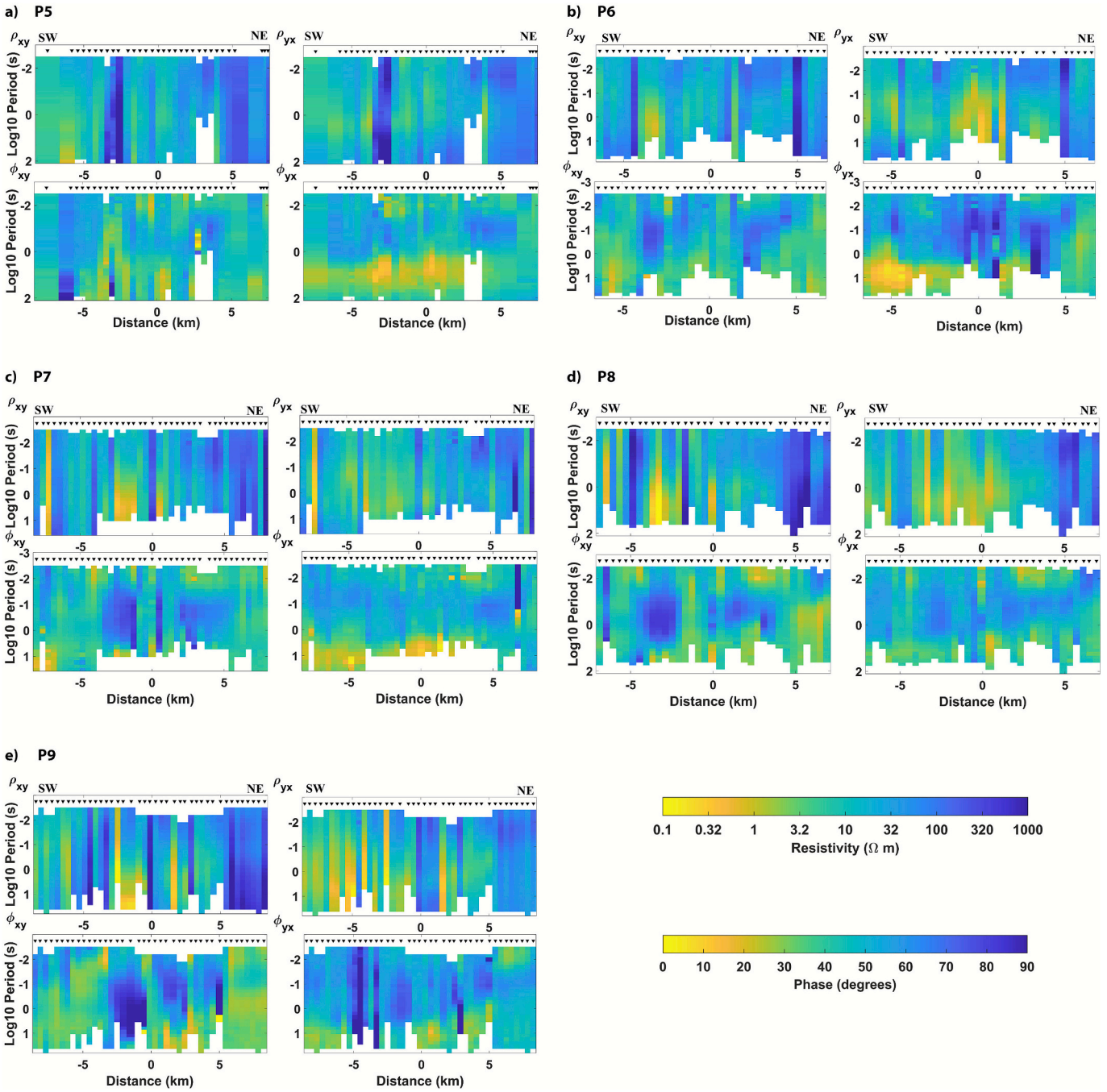

Fig. 4. Apparent resistivity (top row) and impedance phase (bottom row) from the Z_{xy} (left) and Z_{yx} (right) impedance components for each site of the MT array. These are displayed in pseudo-sections along five profiles (a–e; profile 5, 6, 7, 8, and 9). The Z_{xx} and Z_{yy} components are shown in Fig. S1 of the Supplementary Material.

ϕ_{min}, and α-β magnitudes using an ellipse (Caldwell et al., 2004). The different forms of the phase tensor can be represented by their actual shape or by normalizing the large axis with other values such as ϕ_{max} or $1/\phi_{max}$.

In a 1D subsurface, the phase tensor is reduced to a circle ($\phi_{max} = \phi_{min}$) with β equal to zero. In a 2D subsurface, β is close to zero and the strike direction aligns with one principal axis (ϕ_{max} or ϕ_{min}). In a 3D subsurface, the phase tensor is characterized by large values of β and plots as an ellipse. Phase splitting — i.e., large differences between the values of ϕ_{max} and ϕ_{min} — can be diagnostic of the presence of electrical anisotropy (e.g., Heise et al., 2006; Martí, 2014). This can be visualized as an elongated phase tensor ellipse or one with highly contrasting colours. Often this pattern is consistent over a large area. However, phase splitting can also be caused by lateral variations in resistivity from 2D isotropic structures (e.g., edge of a fault zone), although these effects may be very localized.

The phase tensor magnitudes for each station and each period are shown as pseudo-sections for each profile in Fig. 5. In general, at short periods (e.g., less than 1 s; which represent shallow depths) most stations show ellipses that represent 1D and 2D structures, whereas at longer periods 3D structures appear. At periods of about 0.03–1 s the phase tensor magnitudes are more than 45° and at periods of 1–100 s the phase tensor magnitudes are generally less than 45°. This implies that the data are sensing structures at greater depths that have a higher

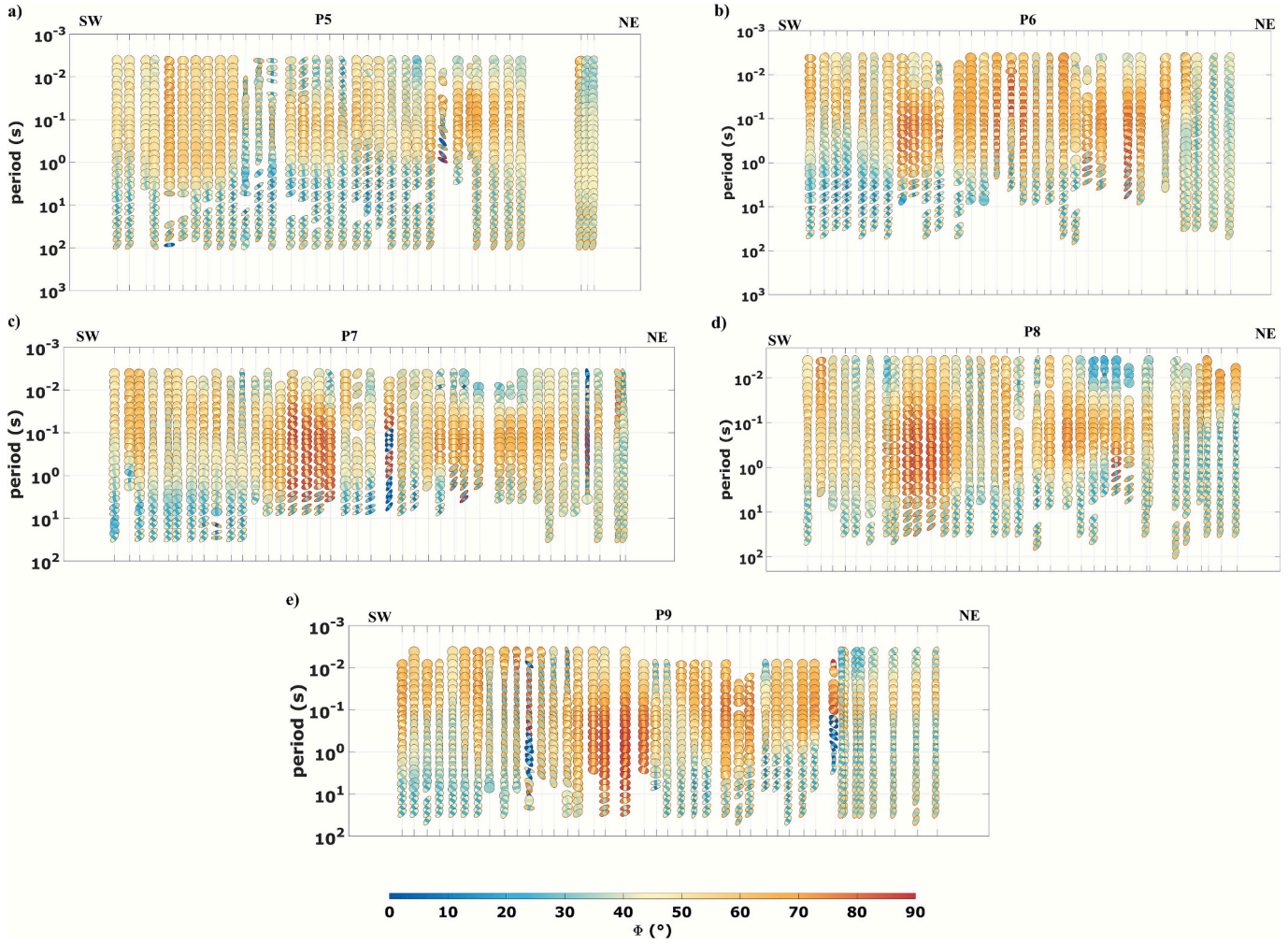

Fig. 5. Phase tensor (PT) for each site of the MT array. These are displayed as pseudo-sections along five profiles (a–e). The ellipses are filled with a colour representing ϕ_{max} and a coloured bar represents ϕ_{min}.

electrical resistivity.

The resistivity phase tensor (RPT) was introduced by Hering et al. (2019) and can be used to determine the dimensionality of subsurface structures. In a pure 1D structure, $\phi_{a,max} = \phi_{a,min}$ (the principal axes) and it can be graphically represented by a circle. There are two modes when structure is 2D: $\alpha = 0^\circ$ and $\beta = 0^\circ$, $\alpha = 90^\circ$ and $\beta = 0^\circ$. Where β defines the position of the major axis relative to a reference axis, and α defines the position of the reference axis relative to the coordinate axes.

As can be seen in Fig. 6, for all profiles between 0.03 and 1 s, a relatively low resistivity structure is implicated by the increasing magnitudes of the resistivity phase tensor. Between 1 and 100 s, i.e., at greater depths, the magnitudes are negative and indicate the influence of higher electrical resistivity structures. The relatively low resistivity structure is likely related to the Gachsaran Formation (cap rock) and the high resistivity structure is attributed to the Asmari Formation and the deeper Sarvak formation. In this way, the observed data itself helps to identify the boundary between the cap rock and reservoir.

4. Results

4.1. Three-dimensional modelling

In recent years, 3D inversion of MT data has had rapid progress due to advancements in computational power. In this study, we use the ModEM algorithm (Egbert and Kelbert, 2012; Kelbert et al., 2014) to generate 3D electrical resistivity models. We implement a modified version that can account for electrical anisotropy (Kong et al., 2021). This modified version has previously been used on field data by Lee et al. (2024) to explore a region of geothermal potential. Accounting for 3D electrical anisotropy is rarely done, but may hold great potential for new developments. For simplicity we allow only tri-axial anisotropy. In contrast to general anisotropy, tri-axial anisotropy assumes the chosen coordinate system is aligned with the electrical anisotropy axes; therefore, the anisotropy strike, dip, and slant angles are zero. When inverting for electrical anisotropy three resistivities — ρ_x, ρ_y, and ρ_z — are determined at every position (for directions x, y, and z).

For the modelling we used the MT stations with collocated TEM data available for static shift corrections, as these were deemed most reliable. This reduced the available stations to 181 with a maximum spacing of 600 m. A modelling mesh was created with rectilinear cells, having 102 and 122 cells in the horizontal directions (y and x) and 40 cells in the vertical direction (z). The inner part of the mesh had horizontal cell dimensions of 300 m by 300 m (covering an area of approximately 22 by 28 km), and in the outer part (15 padding cells in every direction) the dimensions increased geometrically at a rate of 1.5 in both directions. Vertical cell dimensions started with a thickness of 20 m (just below the surface) and increased geometrically at a rate of 1.2 downwards (z direction). This gives vertical cell dimensions >200 m at depths >1000 m.

All four complex components of the impedance tensor were used for the inversion. Data within a range of 0.003–100 s were used, with 31 discrete periods (logarithmically spaced). Data errors were used in

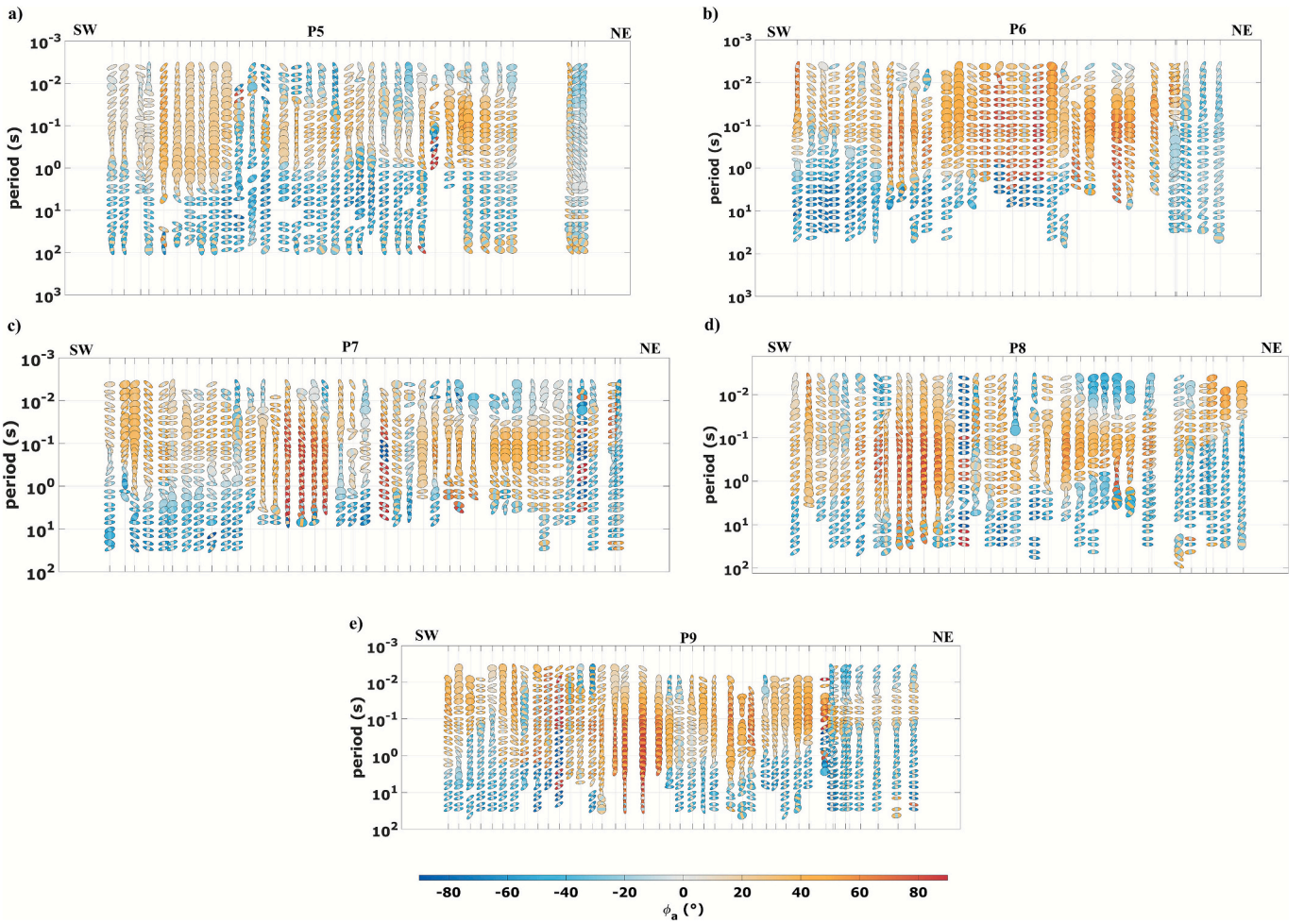

Fig. 6. Resistivity phase tensor (RPT) for each site of the MT array. These are displayed as pseudo-sections along five profiles (a–e). The ellipses are filled with a colour representing the value of the major axis and a coloured bar represents the value of the minor axis.

combination with an error floor of 5 % of $\sqrt{|Z_{xy}Z_{yx}|}$ for the off-diagonal impedance components and 10 % of $\sqrt{|Z_{xy}Z_{yx}|}$ for the diagonal components. Choices for the above values were based on many studies that have used the ModEM algorithm in both similar and different environments (Ślęzak et al., 2019; Robertson et al., 2020; Comeau et al., 2021; Wang et al., 2022; Sheng et al., 2023; Unsworth et al., 2023; Boukhalfa et al., 2024).

To test the robustness of the model, various parameters must be tested in different model runs, such as the model covariance and the starting model resistivity. The covariance parameter controls the smoothness or roughness of the inverted subsurface resistivity model, acting as a regularization term to balance fitting the observed data versus producing a geologically simple model (for more detail see Robertson et al., 2020). Covariance parameters from 0.2 to 0.7 were tested. The fit of the model to the data was computed as a normalized root mean square (nRMS) misfit. Overall, the model misfit was reduced from a starting value of 39 to a final value of 2.0–2.8 within 118–149 iterations. Table S1 shows the misfit and number of iterations for each model and Fig. S3 of the Supplementary Material shows the resulting electrical resistivity models. The model with a covariance parameter of 0.5 provided the best data fit and appeared to be geologically plausible and was thus chosen as the final model.

It is optimal to choose a starting model resistivity near the average resistivity value of the dataset. For testing this parameter, modelling tests were carried out with starting models that consisted of a homogenous half-space with 1, 10, 100, and 1000 Ωm. The results of these tests showed that a homogeneous half-space of 100 Ωm was able to best represent the average resistivity value of the data. The prior model was the same as the starting model (typical with the ModEM algorithm). All models used the same initial damping factor lambda, which was equal to 10 (for all directions; Kong et al., 2021).

The nRMS values for each site and each component of the impedance tensor as well as total values of nRMS for the anisotropic inversion are shown in Fig. 7. For comparison, the nRMS values are also displayed for the isotropic inversion in Fig. 8. The anisotropic inversion had 135 iterations and a final total nRMS misfit of 2.02, having decreased from a starting nRMS of 39.2. The isotropic inversion ran for 93 iterations and achieved a final total nRMS misfit of 2.89, having decreased from a starting nRMS of 39.2. The nRMS values for each iteration of the isotropic and anisotropic inversions (the convergence curve) is shown in Fig. S4 of the Supplementary Material.

4.2. *Comparison of isotropic and anisotropic models*

The isotropic 3D electrical resistivity model and the anisotropic model are illustrated in Fig. 9. The (triaxial) anisotropic model has three resistivity values, ρ_x, ρ_y, and ρ_z, that are aligned with the model coordinate system axes (x, y, and z). In this study the coordinate system axes (x, y, and z) are defined to be along the profiles, across the profiles, and downwards, respectively. There are visible differences in the modelled structures and resistivity values between the isotropic and anisotropic models. The nRMS misfit value in the anisotropic model is lower than in

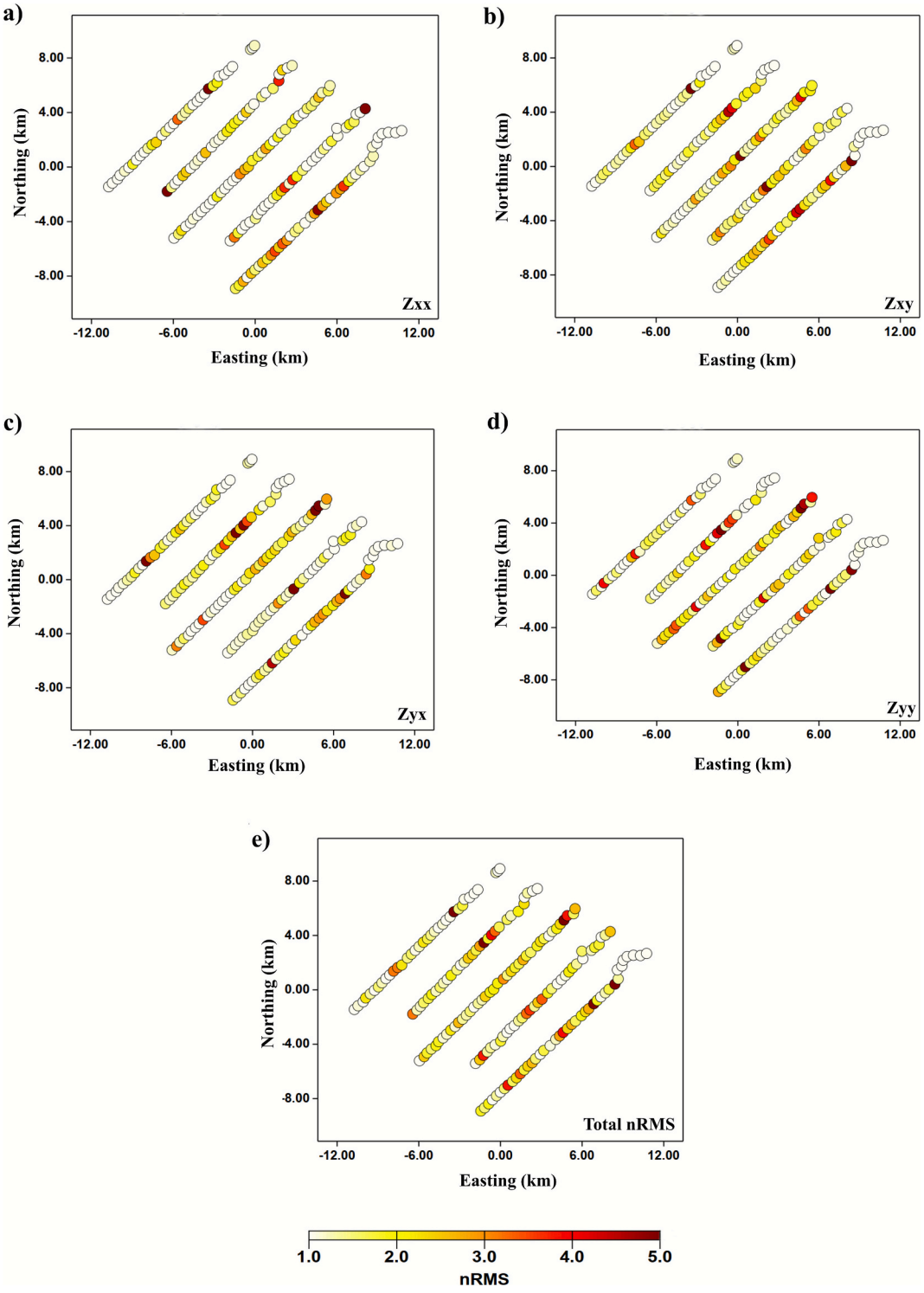

Fig. 7. The nRMS misfit for each site and each component of the impedance tensor from the anisotropic 3D electrical resistivity model. The nRMS values for (a) Z_{xx}, (b) Z_{xy}, (c) Z_{yx}, (d) Z_{yy}, and (e) the global nRMS.

the isotropic model, suggesting a better fit of the final model to the measured data. However, it should be emphasized that a lower nRMS value does not necessarily indicate a more accurate representation of the subsurface structures.

Because one of the objectives of this research is to define the boundary between the Gachsaran and Asmari formations with electrical resistivity models, we examine which model best fits the available drilling data and geological information. Along profile 7, four wells have been drilled, with the relevant data summarized in Table 1 (Sarvandani et al., 2017). It was observed that the top of the Asmari formation is located at depths of approximately 2400 m (Well 1 and 2), 2164 m (Well 3), and 2535 m (Well 4) below surface. Above this, the Gachsaran formation is observed with a thickness of approximately 800–2500 m. The observed variations in formation thickness and depth among the wells indicate lateral and vertical heterogeneities within the subsurface, which may be attributed to structural deformation such as folding,

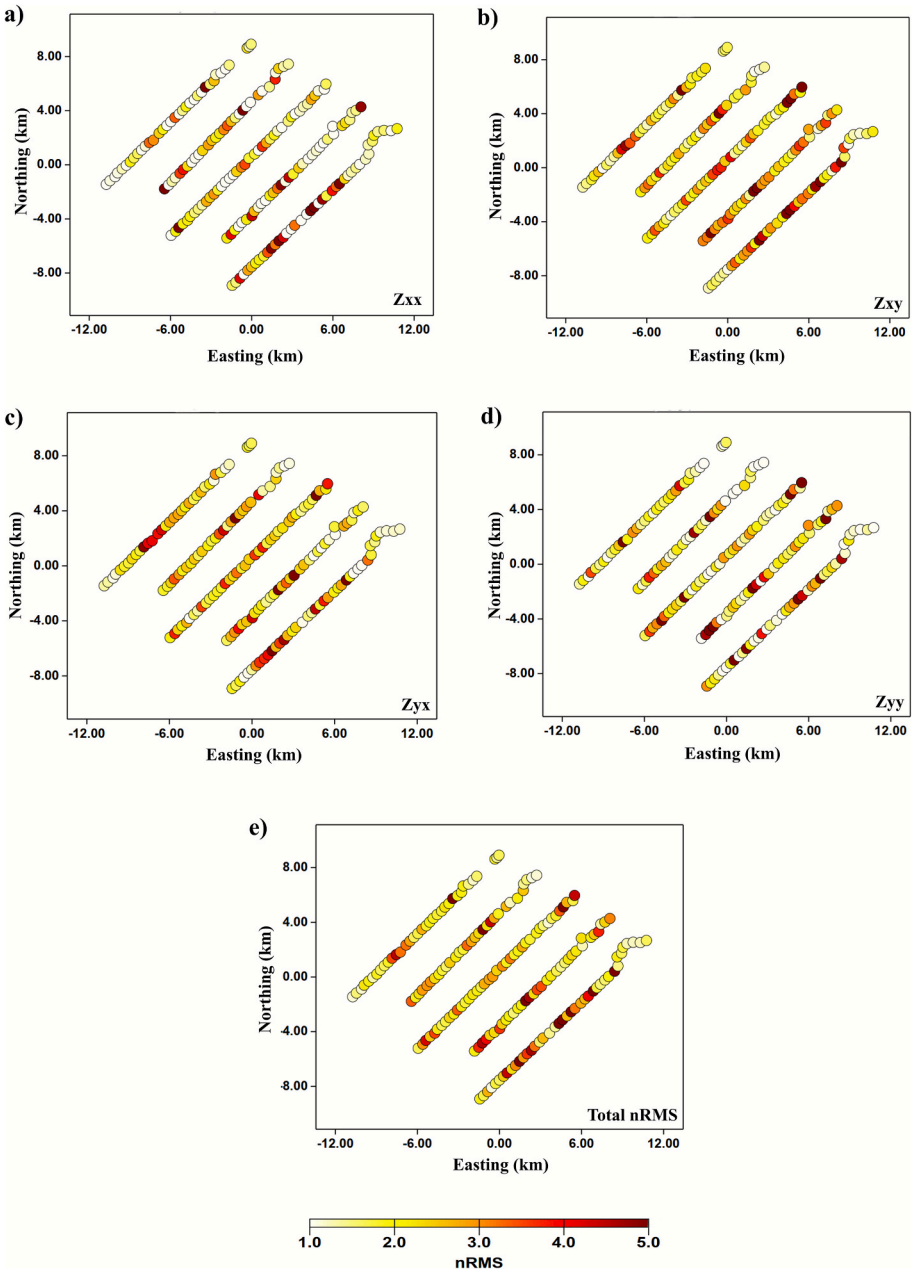

Fig. 8. The nRMS misfit for each site and each component of the impedance tensor from the isotropic 3D electrical resistivity model. The nRMS values (a) Z_{xx}, (b) Z_{xy}, (c) Z_{yx}, (d) Z_{yy}, and (e) the global nRMS.

faulting, or differential subsidence. These structural complexities are likely related to regional tectonic processes.

The model for ρ_y exhibits the best correlation with the drilling data. That is, it best delineates the boundary of the bottom of the Gachsaran formation (the primary cap rock) and the top of Asmari formation (the principal reservoir) through the strong contrast in electrical resistivity, from relatively low to high electrical resistivity. The y-direction is oriented perpendicular to the profiles, south-eastward; it is oriented approximately parallel to the principal geological features (e.g., the fault zones).

5. Description and discussion

5.1. General description

The results of the 3D electrical resistivity modelling were shown for an isotropic model and anisotropic models (with ρ_x, ρ_y, and ρ_z) in Fig. 9. As noted above, the anisotropic model for ρ_y exhibits the best correlation with the drilling data and the expected geological formations. Thus, for conciseness and simplicity, we focus on interpretation of this profile. The results from this model are presented along each profile in Fig. 10. Fig. 11 presents the profiles in a 3D view and Fig. 12 shows an isosurface.

To facilitate the interpretation of the results, a geological cross-section is taken as a reference (Fig. 13), which is located between profiles 7 and 8 and is based on drilling data as well as surface geology. A comparison of the resistivity models with the geological cross-section indicates that lithology primarily governs the variations in electrical resistivity. The geological cross-section indicates a sharp boundary between the Gachsaran and Asmari formations, which has been displaced by several faults. The thickness of the Gachsaran Formation ranges from approximately 1500 m to 3000 m. The Asmari Formation has a

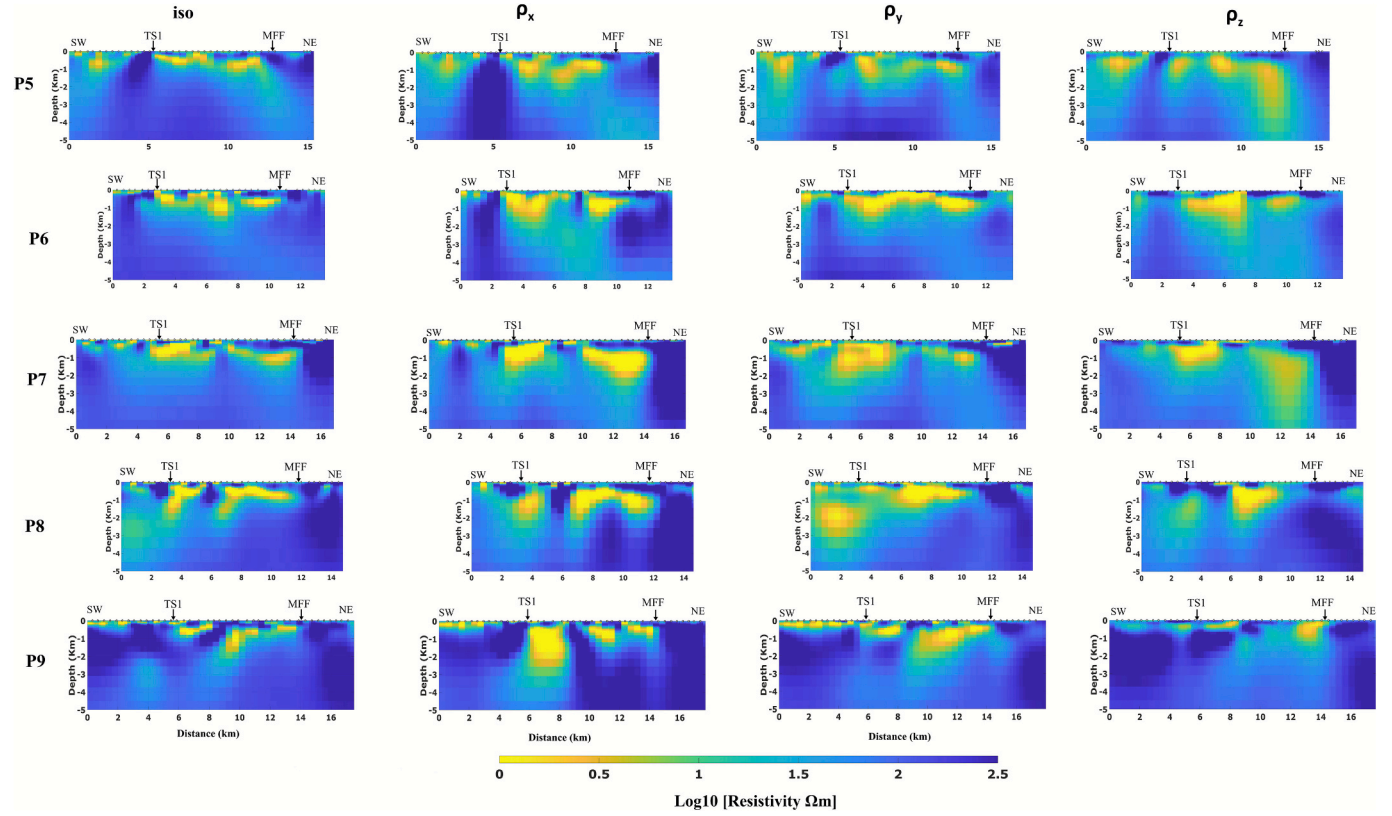

Fig. 9. Vertical sections from the 3D electrical resistivity models, showing the isotropic model (column 1) and anisotropic model (columns 2, 3, and 4, for ρ_x, ρ_y, and ρ_z, along profile, across profile, and downwards) along five profiles of the MT array (rows; profiles 5, 6, 7, 8, and 9).

Table 1
Information about formation boundaries from drilled wells (N.I.S.O.C., 2001; Sarvandani et al., 2017). Note that the surface elevation varies from approximately 810 m above sea level (a.s.l.) for Well 1 and 2 to approximately 680 m a.s.l. for Well 3 and 4.

	Formation	Depth (m a.s.l)
Well 1	Gachsaran	770 to −1446
	Asmari	−1584
Well 2	Gachsaran	770 to −900
	Asmari	−1600
Well 3	Gachsaran	−500 to −1280
	Asmari	−1484
Well 4	Gachsaran	677 to −1710
	Asmari	−1855

relatively uniform thickness of approximately 500 m throughout the region. Its top is at a depth below surface of approximately 2000–3000 m. Additionally, the Sarab anticline and the Jafar Abad anticline (possible fluid traps), along with surface synclines, are identified in the central part of the geological cross-section.

Although folds are visible in the region, severe erosion has prevented the surface exposure of parts of faults (e.g., Narimani et al., 2012), limiting the identification of such structures. Nevertheless, in addition to the folds mentioned above, the sudden disappearance of interbedded limestones, the widespread occurrence of salt and anhydrite, and the correlation with discontinuities in adjacent structures have led to the identification of thrust faults TS1 and TS2 (Narimani et al., 2012). Moreover, in the southern outcrop of the Gachsaran Formation, thrust fault TS2 has caused deformation of the Gachsaran Formation. Sepehr et al. (2006) proposed a model for detachment surfaces in the Zagros, demonstrating that deep structures are separated from small-scale surface folds by the thick incompetent detachment layer of the Gachsaran Formation.

The presence of broad-wavelength anticlines with low-angle backlimbs and steep forelimbs in the Dezful Embayment at depth is attributed to the shortening of the Zagros Fold-Thrust Belt (e.g., Sherkati and Letouzey, 2004). To accommodate this shortening and folding, apart from the gravitational and diapiric movements occurring in the region, surface and subsurface structures have formed within the Gachsaran Formation (Narimani et al., 2012). In any case, the development of competent structures and units at depth results in the formation of folds in the upper layers, particularly within the weaker units (Narimani et al., 2012).

Across all profiles, moderate resistive bodies (with resistivity values ranging from 70 to 500 Ωm) are observed at very shallow depths of <1 km (see Figs. 10 and 11). In the southwestern sections, these bodies correspond to the Aghajari Formation; in the central portions of each profile, they are associated with the Mishan and Bakhtiari Formations.

In the northeastern parts of the study area, large resistive bodies (with resistivity values ranging from 100 to 1000 Ωm), which are quite distinct, are observed across all profiles. These features correspond to the Sarvak Formation, which is visible at the surface in the study area. The position of these features is very consistent with the trace of the Mountain Front Fault (see Fig. 10); that is, the features are located northeast of the fault location, and at depth the fault appears to truncate these features with a sharp boundary, indicating its control on the geological layers and formations in this area.

Beneath these resistive bodies, a relatively low resistivity layer with values ranging from 1 to 10 Ωm is identified, varying in thickness across the survey area. This layer corresponds to the Gachsaran Formation. The Gachsaran Formation comprises seven distinct members (see Fig. 2), each likely exhibiting different resistivity values. This variability is clearly reflected in the resistivity model which shows a heterogenous layer (despite this, the individual member units cannot be separated accurately).

It is worth noting that the Gachsaran Formation, which contains

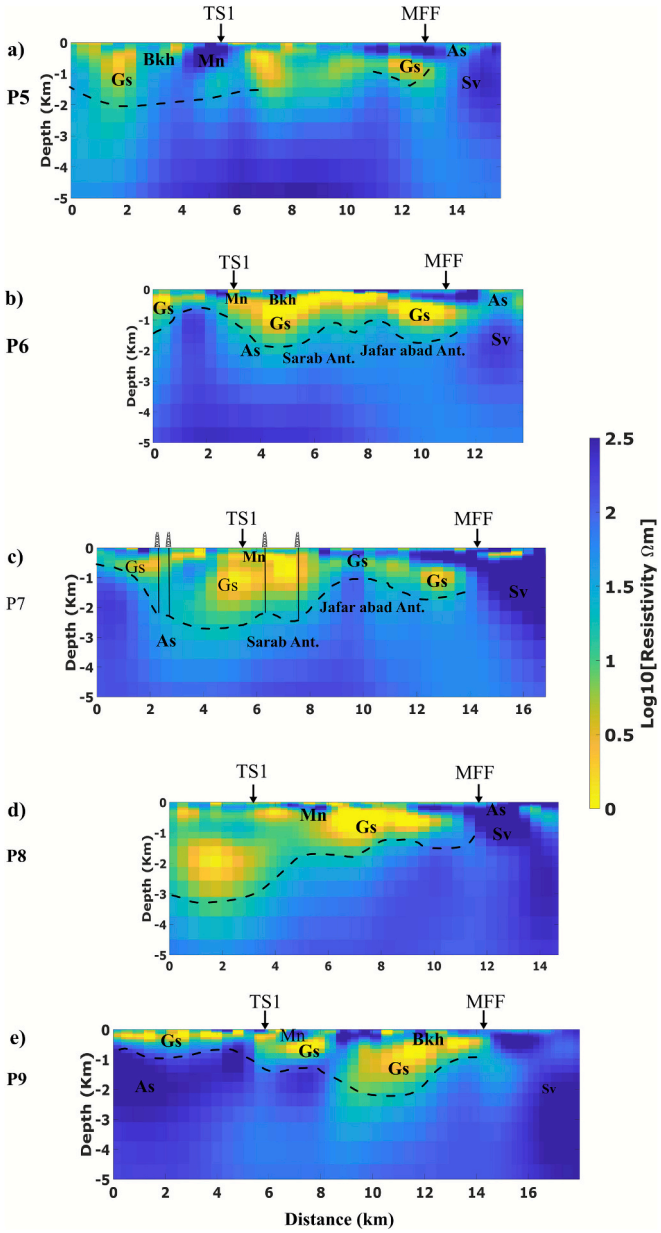

Fig. 10. Electrical resistivity cross-sections from the anisotropic 3D electrical resistivity model for ρ_y along five profiles (each panel, a–e; profile 5, 6, 7, 8, and 9). The acronyms Gs, Aj, Bkh, Sv, and Mn are for the Gachsaran, Aghajari, Bakhtiari, Sarvak, and Mishan formations, respectively. The hypothetical boundary between the Gachsaran Formation and the Asmari Formation is represented by dashed lines. Four drilling wells are shown on profile 7 (panel c).

evaporite-rich stratigraphic layers including anhydrite (an evaporite mineral related to the deposition of brines in sedimentary basins) interbedded with other materials including marl (a clay and carbonate-rich mudstone), has a relatively low electrical resistivity. This is in contrast to massive salt structures (salt domes or diapirs) that are composed of halite (i.e., rock salt), which are well known in central Iran as well as the Gulf Coast of North America, and that, when dry, exhibit a very high electrical resistivity (Key et al., 2006; Filbandi Kashkouli et al., 2025).

The next layer, which is located below the Gachsaran Formation, corresponds to the Asmari Formation. This layer exhibits resistivity values ranging from 50 to 80 Ωm. Thus it has a higher electrical resistivity than the layer above it. This formation, composed of limestone

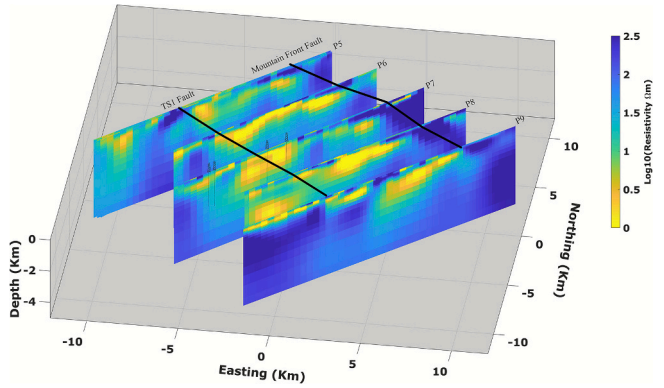

Fig. 11. A 3D perspective view of the study area across the Sarab field with vertical slices from the anisotropic 3D electrical resistivity model for ρ_y. The Mountain Front Fault and TS1 Fault are marked by black lines. Four drilling wells are shown on profile 7.

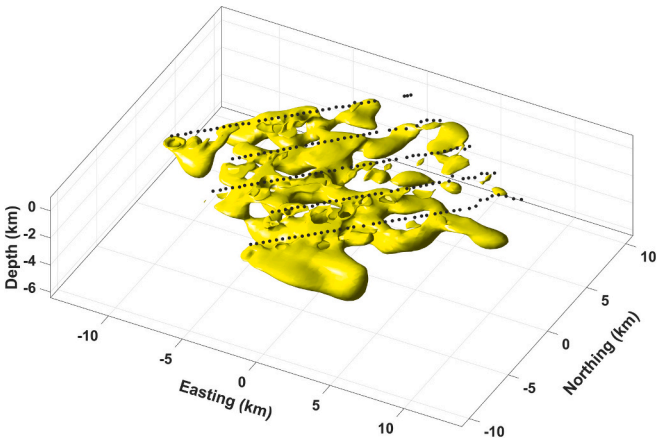

Fig. 12. An isosurface of 10 Ωm from the ρ_y model highlights the variability in the conductor interpreted to be the Gachsaran formation across the survey area. The black circles show the MT + TEM measurement locations.

and dolomitic limestone with high porosity and permeability, is recognized as one of the most important hydrocarbon reservoirs in the Zagros Fold and Thrust Belt (e.g., James and Wynd, 1965).

5.2. *Detailed description of each profile*

5.2.1. *Profile 5*

At depths of 0–1000 m along this profile, the Bakhtiari and Mishan Formations are observed 4–6 km from the profile starting point. The Mishan Formation, at depths of 0–200 m, has surfaced as a result of the activity of the TS1 fault. This structural displacement highlights the significant role of the TS1 fault in bringing formations, such as the Mishan, to the surface along the profile. In the northeastern segment of the profile, the activity of the MFF has caused the Asmari and Sarvak Formations to reach the surface. The Gachsaran Formation exhibits a greater thickness in the southwestern segment of the profile compared to its northeastern segments. Its thickness may reach beyond 2000 m in the southwestern area. At shallow depths in the central area, the electrical resistivity is moderately low rather than low (as in the southwestern and northeastern segments) and thus this area is thus difficult to attribute to the Gachsaran Formation.

5.2.2. *Profile 6*

Along this profile, at depths of 0–500 m the activity of the TS1 and MFF faults has resulted in the presence of the Mishan, Asmari, and

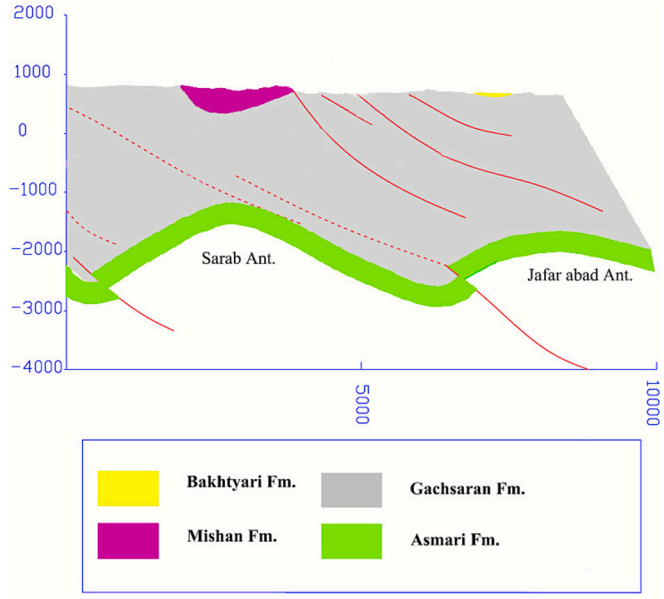

Fig. 13. Geological cross-section. It is located between profile 7 and profile 8 and runs parallel to them, see map in Fig. 1. The boundary between the Gachsaran formation (grey) and Asmari formation (green) can be seen. The Sarab anticline and Jafar Abad anticline are shown. Red lines (dashed and solid) are fault zones. The surface locations of the TS1 fault and the TS2 fault are indicated. Note that the surface elevation across the section varies from approximately 810 to 660 m above sea level. (For interpretation of the references to colour in this figure legend, the reader is referred to the web version of this article.)

Sarvak formations in the southwestern and northeastern segments, respectively. The maximum thickness of the Gachsaran Formation along this profile is approximately 2000 m. The distinct resistivity values of the Gachsaran Formation's members make it somewhat heterogenous. The depth of the Asmari Formation at a distance of 11 km from the profile starting point has decreased abruptly due to the activity of the MFF fault. This sudden change highlights the significant influence of fault activity on the stratigraphic architecture and structural deformation along the profile. The Sarab anticline and the Jafar Abad anticline are clearly observed 6–10 km from the profile starting point.

5.2.3. Profile 7

Based on geological data and the obtained electrical resistivity model, we can deduce that the formations along this profile exhibit distinct geological and tectonic characteristics. The Mishan Formation is observed at the surface 6–8 km from the start of the profile at depths of 0–250 m, likely due to the activity of the TS1 fault. The Bakhtiari Formation outcrops across the profile at similar depths, while the Gachsaran Formation shows a variable thickness ranging from 500 to 3000 m. In the northeastern section, the activity of the MFF fault has caused the Sarvak and Asmari Formations to reach the surface. Additionally, the Sarab anticline and the Jafar Abad anticline are identified 6–12 km from the profile starting point. The significant contrast in resistivity values between the Gachsaran and Asmari Formations (as well as between the Asmari Formation and the underlying layers such as the Sarvak), is a critical factor for delineating the boundary between these formations. This boundary is represented by dashed lines in the interpreted sections (Fig. 10). The depth to the top of the Asmari formation identified in the drilling data (see Table 1) is consistent with the inferred depth from the electrical resistivity model.

5.2.4. Profile 8

In this profile, the Mishan Formation is likely observed in the central part at depths of 0–400 m, influenced by the activity of the TS1. The Asmari and Sarvak Formations, due to the MFF fault, emerge at the surface in the northeastern end of the profile. Unlike profiles 5, 6, and 7, the Gachsaran Formation along this profile has a significant thickness, reaching up to approximately 3000 m in the southwestern section. This thickness gradually decreases towards the northeast, reducing to about 1200 m at a profile distance of 11 km. The Asmari Formation has a thickness of approximately 500 m along this profile and, based on its resistivity, is clearly distinguishable from the Gachsaran.

5.2.5. Profile 9

Along this profile, the impacts of the TS1 and MFF faults are clearly evident. The Bakhtiari, Mishan, and Asmari Formations are observed at depths of 0–500 m in the central and northeastern parts of the profile. The Gachsaran Formation exhibits a thickness of approximately 1000 m up to a profile distance of 8 km. Beyond this point, its thickness appears to possibly increase towards 2000 m and then decrease towards the northeast, reaching a thickness of approximately 1000 m at a profile distance of 14 km. This variability in thickness reflects the tectonic and depositional influences along the profile. However, it is possible that the imaged conductor has a smooth bottom in the model, although models that used different covariance parameters (Fig. S3 of the Supplementary Material) showed the same feature.

5.3. Discussion

For the hydrocarbon reservoirs of southwest Iran, knowledge of the precise location of the Gachsaran (cap rock) formation is extremely important for drilling due to evaporites in the formation, which creates significant challenges when accessing the reservoir below. In this study, the Gachsaran formation throughout the study area has been identified based on its relatively low electrical resistivity values. As seen in Figs. 10–12, this formation exhibits varying thicknesses across the area.

When modelling the electrical anisotropy, the anisotropy ratio can be used as a measure to assess the degree of heterogeneity in the Earth's structure. If this ratio equals one, it can be said that the Earth is electrically isotropic; however, values either higher or lower than one indicates the presence of anisotropy in the subsurface structures. Fig. 14 shows the ratio of ρ_x to ρ_y for each profile (Fig. S7 in the Supplementary Material shows the ratio of ρ_z to ρ_y). Along all profiles, the anisotropy ratio is often far from one, which indicates strong electrical anisotropy for some subsurface structures (in particular, those below and between the TS1 and MFF faults).

This is an important result and shows that ignoring electrical anisotropy during inverse modelling, e.g., proceeding with isotropic standard modelling, may result in missing information and inaccurate results (including misplacement of formation boundaries). The causes of electrical anisotropy include layered lithologies, preferential mineral orientation, aligned fractures or microcracks, and fault-related deformation, all of which preferentially guide electrical currents and strongly affect MT responses (e.g., Martí, 2014). In regions dominated by evaporites the ductile flow of salt and fault-controlled deformation introduces inherent fabrics and heterogeneities.

The most important tectonic feature of the study area is located in the northeastern section, where a prominent fault zone, the MFF, has caused the underlying formations, especially the Sarvak formation which exhibits very high electrical resistivity values, to be brought to the surface. This was clearly observed across all profiles. The TS1 fault has been identified in the southwestern part of the study area. Evidence shows that it caused the Gachsaran Formation to be uplifted to the surface. The Sarab anticline and the Jafar Abad anticline were imaged in the central section of profile 7, based on their structural information. The results are significant for two main reasons. Firstly, they allow us to better understand the tectonic factors and geological processes influencing the formation and evolution of the region. Secondly, they hold great importance for resource exploration in the Sarab field, and these locations will be of great interest for future exploration.

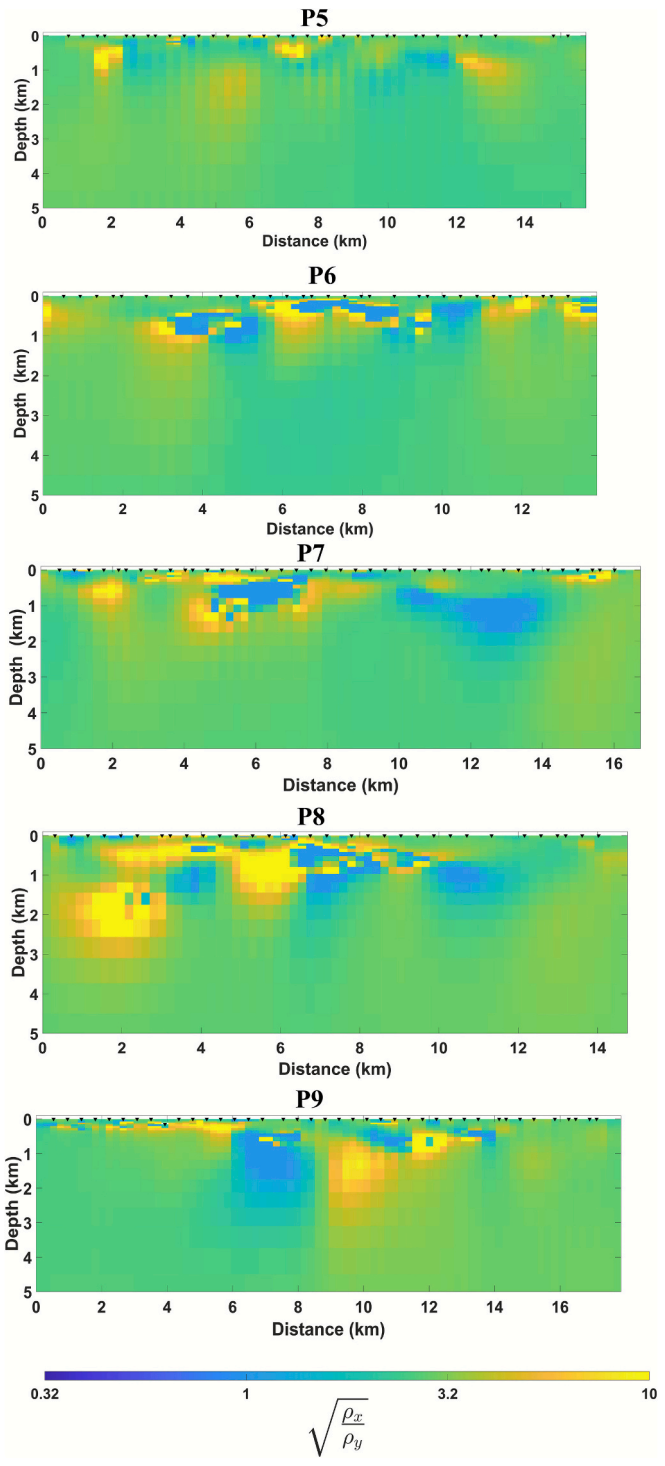

Fig. 14. The of ratio ρ_x to ρ_y gives an impression about the location and strength of electrical anisotropy. Along all profiles (rows), the anisotropy ratio is often far from one.

6. Conclusions

Reservoirs of interest for resource exploration, including geothermal and hydrocarbon reservoirs, commonly have an impermeable cap that traps fluids below. Identifying the depth and location of this boundary, i.e., the top of the reservoir, can be very important. As a case study, we used data from the Sarab field in southwest Iran, where the Gachsaran Formation serves as the primary cap rock and the Asmari Formation is the principal reservoir formation. Knowledge of their interface is of critical significance for drilling; however, past geophysical imaging, specifically using seismic reflection data, faced problems recovering accurate information, largely due to the evaporites in the cap rock formation.

We utilized electromagnetic geophysical data, in the form of MT and TEM measurements, to image the subsurface geological formations. The particular focus was on the Gachsaran and Asmari Formations and the boundary between them. In addition, we sought to gain information about tectonic features and fault zones in order to analyze the tectonic factors influencing the formation of the region as a whole. MT measurements were acquired in array of 12 km by 18 km. At 181 locations, co-located TEM measurements were collected. These were used to control for static shift effects in the MT data. The MT data were analyzed in the form of pseudo-sections of phase tensor and resistivity phase tensor. This revealed a complex resistivity structure but also a clear contrast in phase tensor amplitudes (in the frequency domain) that was identified as the Gachsaran and Asmari Formations.

Fully 3D electrical resistivity models were generated by inverting the MT data, including isotropic models and anisotropic models. Considering 3D electrical anisotropy is rarely done, but ignoring it can result in missing information and inaccurate results. A comparison between the isotropic and anisotropic electrical resistivity models demonstrated that the anisotropic model had a significantly better alignment with the depths of geological formations known from drilling data.

Specifically, among the anisotropic models, it was the model for ρ_y — that is, the model that is oriented approximately parallel to the principal geological features including fault zones — that best fit the drilling data. This model successfully delineated the Gachsaran and Asmari Formations and their boundary, which was our primary goal. This was aided by the fact that the Gachsaran Formation, characterized by its relatively low resistivity, was quite distinct from the Asmari Formation, which exhibited higher resistivity values. We expect that the results and knowledge from our case study with data from the Sarab field can be applied to other regions worldwide and wish to highlight that ignoring electrical anisotropy during inverse modelling may result in missing information and inaccurate results, including misplacement of formation boundaries.

Furthermore, faults and anticlines in the region were identified. This allowed us to analyze the tectonic factors influencing the evolution of the region. The role of faulting in the northeastern part of the study area was clearly observed across all profiles. This is attributed to the MFF that clearly displaced the Sarvak and Asmari Formations. In the southwestern part of the study area, evidence shows that the TS1 Fault caused the Gachsaran Formation to be uplifted to the surface, where it extensively covers the region. Additionally, we were able to characterize and map geological formations including the Sarab anticline and the Jafar Abad anticline in the central part of the study area based on their structural properties. This helps to further our understanding of the geological and tectonic processes that shaped this area and is of great importance to resource exploration of this region and can be applied to other regions.

CRediT authorship contribution statement

Mohammad Filbandi Kashkouli: Writing – review & editing, Writing – original draft, Visualization, Software, Methodology, Formal analysis, Conceptualization. **Matthew J. Comeau:** Writing – review & editing, Visualization, Validation, Software, Methodology, Formal analysis, Supervision. **Milad Farshad:** Writing – review & editing. **Abolghasem Kamkar-Rouhani:** Writing – review & editing.

Funding

This research did not receive any specific grant from funding agencies.

Declaration of competing interest

None.

Acknowledgements

The MT and TEM data for this study were provided by the National Iranian Oil Company. We thank G. Egbert, A. Kelbert, N. Meqbel, and collaborators for the ModEM 3D MT inversion code and W. Kong for graciously providing the anisotropic version. Phase tensor and resistivity phase tensor computations were performed with the FFMT toolbox (C. Castro, P. Hering, and A. Junge; https://www.ffmt.xyz/). Some figures were created with the help of the MT code package (D. Cordell, B. Lee, C. Hanneson, and M. Unsworth; https://doi.org/10.5281/zenodo.6784201). Questions on the study can be addressed to M. Filbandi Kashkouli at kashkoulimohammad@gmail.com.

Appendix A. Supplementary data

Supplementary data to this article can be found online at https://doi.org/10.1016/j.jappgeo.2025.106077.

Data availability

The authors do not have permission to share the data.

References

Agard, P., Omrani, J., Jolivet, L., Mouthereau, F., 2005. Convergence history across Zagros (Iran): constraints from collisional and earlier deformation. Int. J. Earth Sci. 94, 401–419. https://doi.org/10.1007/s00531-005-0481-4.

Al-Farhan, M., Oskooi, B., Ardestani, V.E., Abedi, M., Al-Khalidy, A., 2019. Magnetic and gravity signatures of the Ki oil field in Iraq. J. Pet. Sci. Eng. 183, 106397. https://doi.org/10.22059/IJMGE.2022.342321.594971.

Bedrosian, P.A., Peacock, J.R., Dhary, M., Sharif, A., Feucht, D.W., Zahran, H., 2019. Crustal Magmatism and Anisotropy beneath the Arabian Shield. J. Geophys. Res. Solid Earth 124 (10). https://doi.org/10.1029/2019JB017903.

Berberian, M., 1995. Master 'blind' thrust faults hidden under the Zagros folds: active basement tectonics and surface morphotectonics. Tectonophysics 241, 193–224. https://doi.org/10.1016/0040-1951(94)00185-C.

Boukhalfa, Z., Benhallou, A.Z., Comeau, M.J., Bouzid, A., Bendaoud, A., Deramchi, A., 2024. The structure of a continental intraplate volcanic system and controls from shear zones: insights into the central Hoggar Cenozoic volcanic province, Northwest Africa, from electrical resistivity images. Gondwana Res. 135, 133–150. https://doi.org/10.1016/j.gr.2024.08.003.

Cagniard, L., 1953. Basic theory of the magneto-telluric method of geophysical prospecting. Geophysics 18, 605–635. https://doi.org/10.1190/1.1437915.

Caldwell, T.G., Bibby, H.M., Brown, C., 2004. The magnetotelluric phase tensor. Geophys. J. Int. 158, 457–469. https://doi.org/10.1111/j.1365-246X.2004.02281.x.

Colman-Sadd, S.P., 1978. Fold development in Zagros simply folded belts, Southwest Iran. Am. Assoc. Pet. Geol. Bull. 62, 984–1003. https://doi.org/10.1306/C1EA4F81-16C9-11D7-8645000102C1865D.

Comeau, M.J., Becken, M., Kuvshinov, A.V., Demberel, S., 2021. Crustal architecture of a metallogenic belt and ophiolite belt: implications for mineral genesis and emplacement from 3-D electrical resistivity models (Bayankhongor area, Mongolia). Earth Planets Space 73 (1). https://doi.org/10.1186/s40623-021-01400-9.

Constable, S., Weiss, C.J., 2006. Mapping thin resistors and hydrocarbons with marine EM methods: Insights from 1d modeling. GEOPHYSICS 71, G43–G51. https://doi.org/10.1190/1.2187748.

Edgell, H.S., 1996. Salt tectonics in the Persian Gulf basin. In: Alsop, G.L., Blundell, D.L., Davison, I. (Eds.), Salt Tectonics. Geological Society of London Special Publication. https://doi.org/10.1144/GSL.SP.1996.100.01.10.

Egbert, G.D., Kelbert, A., 2012. Computational recipes for electromagnetic inverse problems. Geophys. J. Int. 189, 251–267. https://doi.org/10.1111/j.1365-246X.2011.05347.x.

Falcon, N.L., 1961. Major earth-flexuring in the Zagros Mountains of south-West Iran. Q. J. Geol. Soc. Lond. 117, 367–376. https://doi.org/10.1144/gsjgs.117.1.0367.

Filbandi Kashkouli, M., Kamkar-Rouhani, A., Arab-Amiri, A., Comeau, M.J., Esmaeili Oghaz, H., 2025. The subsurface structure of salt diapirs revealed with electrical resistivity models in the Shurab area, Central Iran. Tectonophysics 909, 230774. https://doi.org/10.1016/j.tecto.2025.230774.

Gill, W.D., Ala, M.A., 1972. Sedimentology of Gachsaran Formation (lower Fars series), Southwest Iran. Am. Assoc. Pet. Geol. Bull. 56, 1965–1974. https://doi.org/10.1306/819A41A0-16C5-11D7-8645000102C1865D.

Heise, W., Caldwell, T.G., Bibby, H.M., Brown, C., 2006. Anisotropy and phase splits in magnetotellurics. Phys. Earth Planet. Inter. 158 (2), 107–121. https://doi.org/10.1016/j.pepi.2006.03.021.

Hering, P., Brown, C., Junge, A., 2019. Magnetotelluric apparent resistivity tensors for improved interpretations and 3-D inversions. J. Geophys. Res. Solid Earth 124, 7652–7679. https://doi.org/10.1029/2018JB017221.

Hoversten, G.M., 1996. Papua New Guinea MT: looking where seismic is blind. Geophys. Prospect. 44, 935–961. https://doi.org/10.1111/j.1365-2478.1996.tb00185.x.

Hoversten, G.M., Constable, S.C., Morrison, H.F., 2000. Marine magnetotellurics for base-of-salt mapping: Gulf of Mexico field test at the gemini structure. Geophysics 65, 1476–1488. https://doi.org/10.1190/1.1444836.

James, G.A., Wynd, J.G., 1965. Stratigraphical nomenclature of Iranian oil consortium agreement area. Am. Assoc. Pet. Geol. Bull. 49, 2182–2245. https://doi.org/10.1306/A663388A-16C0-11D7-8645000102C1865D.

Johansen, S.E., Amundsen, H., Rosten, T., Ellingsrud, S., Eidesmo, T., Bhuiyan, A.H., 2005. Subsurface hydrocarbons detected by electromagnetic sounding. First Break 23. https://doi.org/10.3997/1365-2397.2005005.

Jones, I.F., Davison, I., 2014. Seismic imaging in and around salt bodies. Interpretation 2. https://doi.org/10.1190/INT-2014-0033.1. SL1–SL20.

Jones, A.G., Chave, A.D., Egbert, G., Auld, D., Bahr, K., 1989. A comparison of techniques for magnetotelluric response function estimation. J. Geophys. Res. Solid Earth 94 (B10), 14201–14213. https://doi.org/10.1029/JB094iB10p14201.

Kelbert, A., Meqbel, N., Egbert, G.D., Tandon, K., 2014. ModEM: a modular system for inversion of electromagnetic geophysical data. Comput. Geosci. 66, 40–53. https://doi.org/10.1016/j.cageo.2014.01.010.

Key, K.W., Constable, S.C., Weiss, C.J., 2006. Mapping 3D salt using the 2D marine magnetotelluric method: Case study from Gemini Prospect. Gulf of Mexico. GEOPHYSICS 71 (1), B17–B27. https://doi.org/10.1190/1.2168007.

Kong, W., Lin, C., Unsworth, M., Tan, H., Lee, B., Peng, M., Wang, M., Tong, T., 2021. Three-dimensional inversion of magnetotelluric data for a resistivity model with arbitrary anisotropy. J. Geophys. Res. Solid Earth 126 (8), e2020JB020562. https://doi.org/10.1029/2020JB020562.

Lee, B., Unsworth, M., Finley, T., Kong, W., Cordell, D., 2024. Electrically anisotropic structure of the Rocky Mountain Trench near Valemount, British Columbia inferred from magnetotellurics: implications for geothermal exploration. Can. J. Earth Sci. 61 (6), 730–749. https://doi.org/10.1139/cjes-2023-0086.

Liang, L., Abubakar, A., Habashy, T.M., 2012. Joint inversion of time-lapse crosswell electromagnetic, seismic, and production data for reservoir monitoring and characterization. Society of Exploration Geophysicists. https://doi.org/10.1190/segam2012-0261.1.

Mahmoodabadi, R.M., 2020. Facies analysis, sedimentary environments and correlative sequence stratigraphy of Gachsaran formation in SW Iran. Carbonates Evaporites 35, 1. https://doi.org/10.1007/s13146-020-00555-y.

Mansoori, I., Oskooi, B., Pedersen, L.B., Javaheri, R., 2015. Three-dimensional modelling of magnetotelluric data to image sehqanat hydrocarbon reservoir in southwestern Iran. Geophys. Prospect. 64, 753–766. https://doi.org/10.1111/1365-2478.12328.

Mansoori, I., Oskooi, B., Pedersen, L.B., 2016. Magnetotelluric signature of anticlines in Iran's sehqanat oil field. Tectonophysics 654, 101–112. https://doi.org/10.1016/j.tecto.2015.05.004.

Martí, A., 2014. The Role of Electrical Anisotropy in Magnetotelluric responses: from Modelling and Dimensionality Analysis to Inversion and Interpretation. Surv. Geophys. 35, 179–218. https://doi.org/10.1007/s10712-013-9233-3.

Martini, F., Hobbs, R., Bean, C., Single, R., 2005. A complex 3D volume for sub-basalt imaging. First Break 23. https://doi.org/10.3997/1365-2397.2005014.

Matsuo, K., Negi, T., 1999. Oil exploration in the difficult minami-noshiro area part 2: Magnetotelluric survey. Lead. Edge 18, 1411–1413. https://doi.org/10.1190/1.1438236.

McQuarrie, N., 2004. Crustal scale geometry of the Zagros fold-thrust belt, Iran. J. Struct. Geol. 26 (3), 519–535. https://doi.org/10.1016/j.jsg.2003.08.009.

Melendez Martinez, J., Schmitt, D.R., 2013. Anisotropic elastic moduli of carbonates and evaporites from the Weyburn-Midale reservoir and seal rocks. Geophys. Prospect. 61, 363–379. https://doi.org/10.1111/1365-2478.12032.

Moorkamp, M., Heincke, B., Jegen, M., Hobbs, R.W., Roberts, A.W., 2016. Joint Inversion in Hydrocarbon Exploration. In: Integrated Imaging of the Earth: Theory and Applications, American Geophysical Union. John Wiley & Sons, Inc. https://doi.org/10.1002/9781118929063.ch9

Motiei, H., 1995. Geology of Iran, Petroleum Geology of Zagros: Geological Survey of Iran. In Persian.

Murris, R.J., 1980. Middle East: stratigraphic evolution and oil habitat. Am. Assoc. Pet. Geol. Bull. 64, 597–618. https://doi.org/10.1306/2F918A8B-16CE-11D7-8645000102C1865D.

Narimani, H., Yassaghi, H., Hasan-Godarzi, M., 2012. Structural analysis of the Dogonbadan area; the Zagros Fold-Thrust Belt, evidence of the frontal and lateral ramp. Scientific Quarterly Journal of Geosciences 21 (82), 53–64. https://doi.org/10.22071/gsj.2011.54440.

N.I.S.O.C., 2001. Final reports of wells in the Gachsaran region.

O'B Perry, J.T., Setudehnia, A., 1966. Masjed-e-Suleyman, Scale 1:100,000. Iranian Oil Oper. Co., Tehran.

Rajab, J.S.A., Tarazi, E.A., 2017. Illuminating and optimising a three-dimensional model of an oil shale seam and its volume distribution using the transient electromagnetic induction method, central part of Jordan. Geophys. Prospect. 66, 603–625. https://doi.org/10.1111/1365-2478.12547.

Robertson, K., Thiel, S., Meqbel, N., 2020. Quality over quantity: on workow and model space exploration of 3D inversion of MT data. Earth Planets Space 72. https://doi.org/10.1186/s40623-019-1125-4.

Sarvandani, M.M., Kalateh, A.N., Unsworth, M., Majidi, A., 2017. Interpretation of magnetotelluric data from the Gachsaran oil field using sharp boundary inversion. J. Pet. Sci. Eng. 149, 25–39. https://doi.org/10.1016/j.petrol.2016.10.019.

Sepehr, M., Cosgrove, J., Moieni, M., 2006. The impact of cover rock rheology on the style of folding in the Zagros fold-thrust belt. Tectonophysics 427 (1–4), 265–281. https://doi.org/10.1016/j.tecto.2006.05.021.

Sheng, Y., Jin, S., Comeau, M.J., Hou, Z., Becken, M., Dong, H., et al., 2023. Evidence for partial melting and alkali-rich fluids in the crust from a 3-D electrical resistivity model in the vicinity of the Coqen region, western Lhasa terrane, Tibetan Plateau. Earth Planet. Sci. Lett. 619, 118316. https://doi.org/10.1016/j.epsl.2023.118316.

Sherkati, S., Letouzey, J., 2004. Variation of structural style and basin evolution in the central Zagros (Izeh zone and Dezful embayment), Iran. Mar. Pet. Geol. 21 (5), 535–554. https://doi.org/10.1016/j.marpetgeo.2004.01.007.

Ślęzak, K., Jozwiak, W., Nowozynski, K., Orynski, S., Brasse, H., 2019. 3-D studies of MT data in the central Polish Basin: Influence of inversion parameters, model space and transfer function selection. J. Appl. Geophys. 161, 26–36. https://doi.org/10.1016/j.jappgeo.2018.11.008.

Strack, K.M., 2014. Future directions of electromagnetic methods for hydrocarbon applications. Surv. Geophys. 35, 157–177. https://doi.org/10.1007/s10712-013-9237-z.

Strack, K.M., Hoerdt, A., Wolfgram, P.A., Vozoff, K., 1991. Integrated electromagnetic and seismic methods for petroleum exploration. Explor. Geophys. 22, 375–378. https://doi.org/10.1071/EG991375.

Sun, L., Fang, C., Sa, L., Yang, P., Sun, Z., 2015. Innovation and prospect of geophysical technology in the exploration of deep oil and gas. Pet. Explor. Dev. 42, 454–465. https://doi.org/10.1016/S1876-3804(15)30038-0.

Takin, M., 1972. Iranian geology and continental drift in the middle east. Nature 235, 147–150. https://doi.org/10.1038/235147a0.

Talebian, M., Jackson, J., 2002. Offset on the Main recent Fault of NW Iran and implications for the late Cenozoic tectonics of the Arabia-Eurasia collision zone. Geophys. J. Int. 150 (2), 422–439. https://doi.org/10.1046/j.1365-246X.2002.01711.x.

Tikhonov, A.N., 1950. On determining electrical characteristics of the deep layers of the Earth's crust. Doklady 73, 295–297.

Travassos, J.M., Menezes, P.T.L., 1999. Geoelectric structure beneath limestones of the Sao Francisco Basin, Brazil. Earth Planets Space 51, 1047–1058. https://doi.org/10.1186/BF03351578.

Unsworth, M., Comeau, M.J., Diaz, D., Brasse, H., Heit, B., Favetto, A., et al., 2023. Crustal structure of the Lazufre volcanic complex and the southern Puna from 3-D inversion of magnetotelluric data: Implications for surface uplift and evidence for melt storage and hydrothermal fluids. Geosphere 19 (5), 1210–1230. https://doi.org/10.1130/GES02506.1.

Wang, T., Ma, G., Comeau, M.J., Becken, M., Zhou, Z., Liu, W., et al., 2022. Evidence for the superposition of tectonic systems in the northern Songliao Block, NE China, revealed by a 3-D electrical resistivity model. J. Geophys. Res. Solid Earth 127 (4). https://doi.org/10.1029/2021JB022827.

Watts, M.D., Pince, A., 1998. Petroleum exploration in overthrust areas using magnetotelluric and seismic data. Society of Exploration Geophysicists. https://doi.org/10.1190/1.1820454.

Xiao, W., Unsworth, M., 2006. Structural imaging in the Rocky Mountain Foothills (Alberta) using magnetotelluric exploration. AAPG Bull. 90, 321–333. https://doi.org/10.1306/10150504140.

Yilmaz, Oz, 2001. Seismic Data Analysis: Society of Exploration Geophysicists.

Zhang, K., Wei, W., Lu, Q., Dong, H., Li, Y., 2014. Theoretical assessment of 3-D magnetotelluric method for oil and gas exploration: Synthetic examples. J. Appl. Geophys. 106, 23–36. https://doi.org/10.1016/j.jappgeo.2014.04.003.

Zhdanov, M.S., Wan, L., Gribenko, A., Čuma, M., Key, K., Constable, S., 2011. Large-scale 3D inversion of marine magnetotelluric data: Case study from the Gemini prospect. Gulf of Mexico. GEOPHYSICS 76 (1), F77–F87. https://doi.org/10.1190/1.3526299.